Received: 15 July 2022 | Revised: 20 November 2022 | Accepted: 19 December 2022

DOI: 10.1002/pip.3665

SPECIAL ISSUE ARTICLE

PROGRESS IN PHOTOVOLTAICS WILEY

# Novel semi-transparent solar cell based on ultrathin multiple Si/Ge quantum wells

Hosni Meddeb[1] | Maximilian Götz-Köhler[1] | Christoph Flathmann[2] | Michael Seibt[2] | Kai Gehrke[1] | Martin Vehse[1]

[1]Institute of Networked Energy Systems, Urban and Residential Technologies, German Aerospace Center (DLR), Oldenburg, Germany

[2]Institute of Physics – Solids and Nanostructures, University of Goettingen, Göttingen, Germany

**Correspondence**
Hosni Meddeb, Institute of Networked Energy Systems, Urban and Residential Technologies, German Aerospace Center (DLR), Carl-von-Ossietzky-Str. 15, Oldenburg 26129, Germany.
Email: hosni.meddeb@dlr.de

**Funding information**
German Aerospace Center (DLR); Deutsche Forschungsgemeinschaft (DFG, German Research Foundation), Grant/Award Number: 217133147/SFB 1073

## Abstract

Unlike conventional opaque solar cells, semi-transparent solar cells enable simultaneous electricity generation and light transmission. Along with solar energy harvesting, the offered multiple functionalities of these technologies, such as aesthetic appearance, visual comfort and thermal management, open diverse integration opportunities into versatile technological applications. In this work, the first demonstration of a novel semi-transparent solar cell based on ultrathin hydrogenated amorphous Si/Ge multiple quantum wells (MQW) is reported. Through optoelectronic modelling, the advantages of ultrathin MQW as photoactive material to overcome the intrinsic limitations of thin (20 nm) and ultrathin (2.5 nm) single quantum well (SQW) counterparts are explained. This allows extra degree of freedom for both optical design and bandgap engineering. Mainly, the multiplication of the QWs number in a periodic configuration, taking advantage of effective synergy between electronic and photonic confinements, leads to an improvement of photocurrent, while preserving high voltage and fill factor and ensuring significant transparency. The MQW new concept yields a boost in power conversion efficiency up to 3.4% and a considerable average visible transmission of about 33%. A light utilization efficiency above 1.1% is achieved, which can be considered as one of the highest among inorganic semi-transparent solar cell technologies. The successful demonstration of ultrathin semi-transparent Si/Ge MQW solar cells indicates the promising integration potential of this emerging photovoltaic technology for supplying systems in relevant applications such as in buildings, vehicles and greenhouses.

**KEYWORDS**
bandgap engineering, nanophotonic structure, nanotechnology, optoelectronic modelling, quantum confinement, quantum wells, semi-transparent photovoltaics, ultrathin solar cell

## 1 | INTRODUCTION

In contrast to the conventional photovoltaic technologies deployed on residential rooftops and utility scale solar farms, semi-transparent photovoltaics (ST-PV) enable multifunctional characteristics alongside solar energy harvesting such as aesthetic appearance, visual comfort and heat insulation.[1] The customization of the spectral light transmission affords several integration opportunities into diverse applications

like glass façades in buildings and windows and sunroofs in vehicles and greenhouses for agrivoltaics.[1–4]

One of the strategies to achieve ST-PV is to use thin enough photoactive semiconductors with continuous-band absorption that allow partial transmission of a fraction of the incident light over the spectral sensitivity of the human eye in the visible region.[2,3,5] Such ultrathin-film PV technologies can provide promising advantages in terms of low material consumption, fast fabrication processes and cost reduction.[6]

Different inorganic and organic absorbing materials have been employed with various degrees of optical transmission.[5,7] This typically leads to a direct trade-off between the power photoconversion efficiency (PCE) and the average visible transmission (AVT). Among inorganic photoactive materials, hydrogenated amorphous silicon absorbers (a-Si:H) have been widely used in different thin-film ST-PV concepts.[5,7] On the one hand, thickness in the range of hundred nanometres are required to ensure sufficient light absorption and photocurrent level.[5,8] However, this yields a drastic drop in the light transmission.[5,7] On the other hand, ST-PV incorporating ultrathin a-Si:H layer of few nanometres deliver low photocurrent and suffer poor photovoltaic performance.[9–11]

To overcome the absorption limitations of a-Si:H photoactive material, hydrogenated amorphous germanium (a-Ge:H) nanoabsorber, with one of the highest absorption coefficients among other semiconductor materials, is a suitable alternative.[12,13] It enables a drastic thickness reduction by an order of magnitude compared with a-Si:H counterpart down below 20 nm, while still ensuring strong photons absorption. The outstanding achieved photocurrent could surpass other thin-film PV technologies with even thicker photoactive material.[14]

Different ST-PV concepts based on ultrathin a-Ge:H technology have been demonstrated.[15] These include switchable solar cell with gasochromic magnesium back electrode for window applications[16–18] and spectrally selective solar cell with metal/oxide multilayers cavity electrode for greenhouse applications.[19]

Interestingly, another specification of ultrathin a-Ge:H films is the large Bohr radius (approximately 24 nm in Ge compared with only about 5 nm in Si)[20] and, hence, the susceptibility of quantum confinement (QC) effect in low-dimensional nanostructures like in quantum wells (QW) with thicknesses under this fundamental dimension.[21–23] Recently, a successful demonstration of an opaque ultrathin single quantum well (SQW) solar cell based on a-Si:H (barrier)/a-Ge:H (QW) heterostructures embedded as a subwavelength nanophotonic resonator was reported.[24,25] Such concept allows a beneficial synergy between photonic and quantum confinements and a significant thickness-dependent tuning of all the photovoltaic characteristics.[24,26]

On the one hand, thin SQW (~20 nm) with narrow bandgap (Eg ~ 1 eV) yields high short circuit current (Jsc) but suffers from low open-circuit voltage (Voc) and fill factor (FF). On the other hand, ultrathin SQW (~2.5 nm) with wider bandgap (Eg ~ 1.35 eV) is characterized by an opposite trend, resulting in an enhancement of Voc and FF but a drop in Jsc.[24] Considering the high absorption of thicker SQW and the low photogenerated current of ultrathin SQW, it is expected that both SQW configurations would lead to non-optimal trade-off between PCE and AVT in semi-transparent architecture.

In this work, a novel concept for semi-transparent solar cells is explored by integrating ultrathin multiple quantum wells (MQW) based a-Si:H/a-Ge:H nanostructures to overcome the intrinsic limitations imposed by SQW configurations. Based on the conducted optoelectronic modelling, the advantages of ultrathin MQW as photoactive material in terms of photovoltaic performance and transparency, compared with thin SQW (20 nm) and ultrathin SQW (2.5 nm) counterparts, are explained. Experimentally, the boost in power generation and the improvement of the trade-off between efficiency and visible transmission provided by MQW incorporation in ST-PV are confirmed. Therefore, the substitution of SQW by MQW nanoabsorber would be beneficial for rising the performance of different relevant ST-PV, not only static semi-transparent solar cell but also dynamically switchable[16–18] and spectrally selective multifunctional devices.[19]

Furthermore, the outcomes of our findings open new perspectives for further optimization through photonic management and bandgap engineering. This could be achieved by thoroughly studying the design of MQW configurations with different positions, numbers and thicknesses. Moreover, the use of wide-band gap materials as carrier selective contacts can reduce the parasitic absorption and promote the transparency of such MQW ST-PV.[9,10] It is also envisioned that the implementation of quantum dot nanostructures with high degree of QC could offer more pronounced bandgap widening and stronger optical absorption.[20,27–29]

Overall, the proposed new concept of ultrathin Si/Ge MQW semi-transparent solar cell is a promising and efficient device category with significant technological and scientific features.

## 2 | EXPERIMENTAL METHODS

Different SQW and MQW semi-transparent solar cells were fabricated using cost-effective and industrial-compatible processes. A 1-µm-thick aluminium-doped Zinc Oxide ZnO:Al (AZO) transparent conductive oxide layer formed the front contact. The solar cell with n-i-p superstrate configuration consisted of hydrogenated amorphous silicon and germanium multilayers structured as (n-a-Si:H/i-a-Si:H/SQW or MQW/i-a-Si:H/p-a-Si:H) with thicknesses (7 nm/3 nm/SQW or MQW/3 nm/7 nm). The functional layers forming the outer n/i and i/p regions were kept similar for all solar cell devices. The intrinsic regions were composed of an alternation between i-a-Si:H (barrier)/i-a-Ge:H (QW) films. In SQW configurations, only the thickness of a-Ge:H QW nanoabsorber layer is changed. Two different i-a-Ge:H SQW thicknesses were adopted, with ultrathin $L_{QW} = 2.5$ nm and thin $L_{QW} = 20$ nm. For comparison purposes, i-a-Si nanoabsorber of 20 nm composed of full barrier material was also considered. In the multiple QWs region having the same total nanoabsorber thickness as the thin SQW, a periodic stratified medium was incorporated with six QWs of $L_{QW} = 2.5$ nm each, separated by 1-nm-thick quantum barrier (QB) regions. The front contact opening through the glass substrate was performed by laser scribing in microSTRUCTvario system from 3DMicromac. Layer stacks of Ag (15 nm)/AZO (60 nm) were deposited as back transparent electrodes through a shadow mask to define $1 \times 1$ cm$^2$ cell areas.

The front and back electrodes were deposited by DC magnetron sputtering technique, whereas the semiconductor functional layers were fabricated by low-temperature Plasma Enhanced Chemical Vapor Deposition (PECVD) method at 13.56 MHz in the same cluster tool system Von Ardenne CS-400P. Then, all solar cell devices were annealed at 100°C for 30 min. Further details on the fabrication processes can be found in Tables S1 and S2.

The comparison between ultrathin MQW and SQW configurations allows to explore the practical limits in terms of the highest achievable Voc and FF for ultrathin SQW and the highest achievable Jsc for thin SQW.

For the morphological characterization of a-Si/a-Ge MQW multilayers on polished float-zone crystalline silicon (c-Si) substrate, cross-sections have been studied by (scanning) transmission electron microscopy, (S)TEM, using a Titan 80-300 G2 ETEM. TEM lamella preparation was done by standard focused ion beam procedures with a FEI Helios G4. The refractive ($n$) and extinction ($k$) indices of different functional layers were assessed using spectroscopic ellipsometry in SENTECHSE850-ST system. The optical transmission and reflection measurements of the cell devices at normal incidence were carried out using a spectrophotometer Varian 5000 with an integration sphere. External quantum efficiency (EQE) spectra were extracted by means of an in-house differential spectral response setup. Illuminated J-V electrical measurement were conducted using a WACOM dual lamp solar simulator with AM1.5G filter at standard test conditions (1000 mW/cm$^2$, 25°C). The reported experimental results of semi-transparent solar cell devices are determined according to the recommended guidelines in literature.[30]

Through optoelectronic modelling, the experimental device characteristics of different semi-transparent QW solar cells were analysed. The optical modelling was carried out through the implementation of the measured ($n$, $k$) coefficients data for different functional layers into a 1-D transfer matrix method using the software package Scout/CODE (by W. Theiss Hardware and Software). This method, based on wave optics, relates a specific matrix to the propagation of the electromagnetic field (light) through each film of the device. Then, a global matrix is generated for the calculation of the local reflection and transmission coefficients by solving the Fresnel equations at the interfaces between different layers considering the associated matrices to each layer.[31] The electrical numerical simulation was established in AFORSHET software. In this program based on drift-diffusion model, the semiconductor equations including Poisson's, transport and continuity equations for charge carriers are solved.[32] Detailed inputs of the optoelectronic numerical simulation can be found in Table S3 as well as in previous works.[24,26]

## 3 | RESULTS AND DISCUSSIONS

### 3.1 | Structure of semi-transparent ultrathin Si/Ge MQW solar cell

In this part, the functional materials system and the device architecture related to semi-transparent a-Ge:H QW technology are presented. Figure 1A,B illustrates the device structure of semi-transparent solar cells related to thin SQW and multiple ultrathin QWs with the same total nanoabsorber thickness. For both SQW and MQW solar cell devices in Figure 1, the n-i-p region consists of deep-subwavelength lossy a-Si and a-Ge media with high and comparable refractive and extinction indices ($n \sim k$), sandwiched between partially

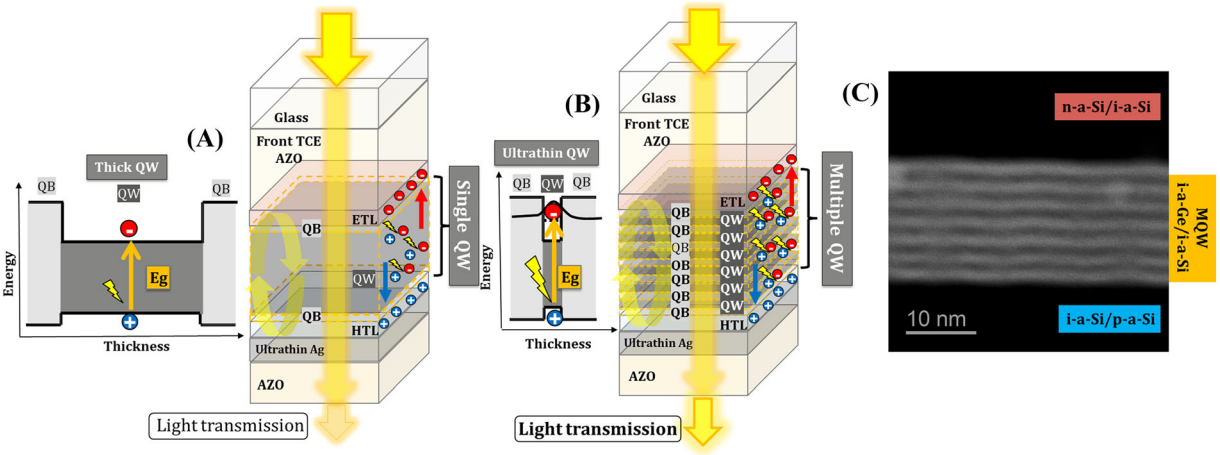


**FIGURE 1** Band alignment in barrier/QW/barrier nanostructures based on a-Si/a-Ge heterojunctions and schematic of semi-transparent ultrathin solar cells for the case of (A) thin single QW and (B) multiple ultrathin QWs. a-Ge:H quantum wells and a-Si:H quantum barriers are denoted by QW and QB, respectively. In the illustrations, QW regions are in dark grey, while QB regions are in bright grey. The path of transmitted light through the cells and the interferences inside the absorbing nanocavity are highlighted by yellow arrows. The photogeneration of electrons and holes charge carriers with photon energy higher than the corresponding QW bandgap is indicated in the energy space and within the device regions. Transport of electrons and holes photogenerated carriers towards the corresponding selective contacts are indicated by red and blue arrows, respectively. (C) STEM cross-section of MQW structure on flat c-Si substrate showing the periodic multilayers based on a-Si/a-Ge nanostructures. Bright and dark regions in STEM image correspond to a-Ge:H and a-Si:H ultrathin layers, respectively. [Colour figure can be viewed at wileyonlinelibrary.com]

reflective AZO front and ultrathin Ag/AZO back electrodes with low refractive indices. This creates a low finesse optical nanocavity where optical interference and photonic confinement occur.

In the illustration of the band alignment corresponding to the multilayer structure, narrow bandgap a-Ge:H QW is embedded between two a-Si:H QB regions. The quantum confinement effect in ultrathin QW in contrast to thin QW leads to an upward shift of the conduction band edge to higher discrete level due to the energy quantization, and hence, a bandgap widening is manifested.[24] This imposes higher photon energy for the photogeneration process within the ultrathin QW regions and the alteration of the band offset at a-Si:H/a-Ge:H heterojunctions.

The STEM cross-section image from a similar structure with the same thin-film deposition parameters (Figure 1C) elucidates the periodic distribution of ultrathin MQW stratified structure composed of alternating amorphous Si-rich (QB) and Ge-rich (QW) layers. Ultrathin a-Ge:H QWs can be clearly distinguished as bright regions, whereas the a-Si:H barriers appear dark in this high-angle annular dark-field (HAADF) image, which further confirms the lateral uniformity of the grown MQW structures.

## 3.2 | Optical modelling of semi-transparent ultrathin Si/Ge MQW solar cell

Within this section, we analyse the expected absorption and the transmission behaviours in semi-transparent ultrathin Si/Ge QW solar cells by means of optical modelling.The main analytical relations governing the optical behaviour semi-transparent ultrathin Si/Ge MQW solar cell are elucidated in Section S3. This includes the relationship between reflection, transmission and absorption.[33,34] The semi-transparent solar cell structures are considered as asymmetric Fabry–Perot nanocavities composed of absorbing a-Si:H and a-Ge:H semiconductor multilayers (medium 2) embedded between transparent front AZO film (medium 1) and Ag/AZO semi-transparent back electrode (medium 3). Then, the equations governing the reflection phase shifts at both nanocavity edges in the vicinity of AZO front electrode and ultrathin Ag/AZO back (or bare air surface) as well as the round-trip propagation across the photonic resonator formed by lossy a-Si:H/a-Ge:H multilayer are established.[35–38] This allows the determination of the resonance condition corresponding to the maximum absorption and minimum reflection, which is typically altered by the change of the refractive index of the back surface, the optical nanocavity length and the effective refractive index of the composing media.

In Section S4, the dispersion spectra of real $n$ and imaginary $k$ parts of the complex indices for different functional materials are presented and interpreted. These $n$ and $k$ data are used as inputs for the optoelectronic modelling.

In addition to the optical refractive indices ($n$, $k$) of materials, the optical absorption in different functional layers across the semi-transparent device mainly depends on the amplitude of light electromagnetic field, given by[34]

$$Absorption\,(z,\lambda) = \frac{2\pi c\,\varepsilon}{\lambda}\, n(z,\lambda) \times k(z,\lambda)\,|E(z,\ \lambda)|^2, \tag{1}$$

where $c$ is the speed of light, $\varepsilon$ is the permittivity of free space and $|E(z,\ \lambda)|^2$ is the electric field amplitude as a function of depth $z$ and wavelength $\lambda$.

In Figure 2, the wavelength dependence of the normalized electric field profile across the depth of different semi-transparent QW solar cells, that is, thin SQW (20 nm), ultrathin SQW (2.5 nm) and MQW (6 × 2.5 nm) devices, is shown. It is observed that the electric field distribution is primarily influenced by the nanoabsorber thickness and, hence, the nanocavity length.[39] An increase of the nanocavity length from ultrathin SQW (2.5 nm) to thin SQW (20 nm) or MQW (6 × 2.5 nm) results in a regression of electric field maxima inside the nanoabsorber regions towards longer wavelengths. Also, the field intensity is influenced by the absorption in the lossy a-Si/a-Ge media as the light is gradually absorbed upon deeper propagation and multiple passes recirculation. Inside the thin SQW (20 nm), the field intensities are low at short wavelengths below 600 nm and rise gradually at longer wavelengths. Within the ultrathin SQW (2.5 nm), the intensities are rather strong over all the wavelengths range. In particular, the spectral range of the electric field with high intensities is extended within MQW (6 × 2.5 nm) region compared with thin SQW (20 nm) with the same nanocavity length.

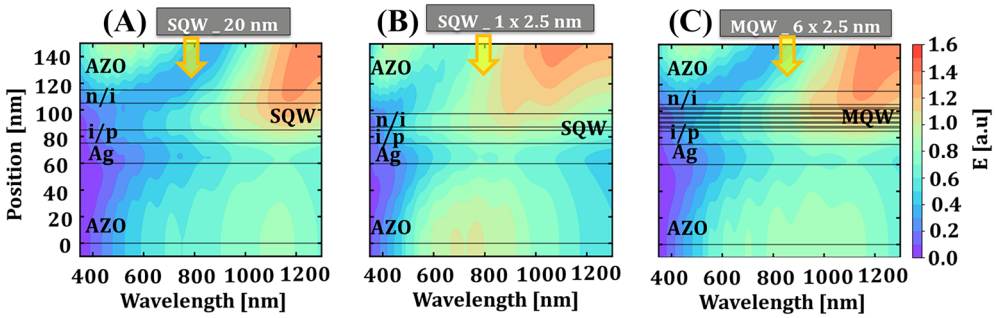


**FIGURE 2** Electric field distributions at perpendicular incidence as a function of light wavelengths and across the depth of semi-transparent solar cells with different nanoabsorber configurations: (A) thin SQW (20 nm), (B) ultrathin SQW (2.5 nm), and (C) ultrathin MQW (6 × 2.5 nm). Yellow arrows indicate the direction of the incident light. [Colour figure can be viewed at wileyonlinelibrary.com]

Moreover, the field distribution is spatially uniform across the total depth of MQW structure at each fixed wavelength. The reason of this alteration in the spectral behaviour of the electric field is mainly due to the fact that the refractive index *n* as a function of wavelength for thin SQW with a-Ge:H layer of 20 nm is different from the effective refractive index evolution of MQW (6 × 2.5 nm) structure where it is rather an average of optical indices of a-Si:H (QB) and a-Ge:H (QW) multilayers weighted by their corresponding thicknesses. This improvement in the distribution of electric field intensity implies a more effective contribution in the optical absorption and hence a beneficial impact in the enhancement of the photocurrent generation.

Interestingly, these observations indicate possible further improvements provided that high electric field intensity favourably coincide with the QW position in the visible wavelengths range. This could be achieved by the optical design of the functional layers at the front side of the device and, particularly, by further optimizing of MQW configuration in terms of positions, numbers and thicknesses.

In Figure 3, taken from the contour plot in Figure 2, we display the electric field intensities variation at selected wavelengths across the depth of semi-transparent solar cell devices for different nanoabsorber configurations. The field maxima in different QW configurations are mostly localized within the QW regions for each individual wavelength. Regarding the transparency aspect, we focus on the field intensity passing through the semi-transparent solar cell devices beyond the outermost AZO back electrode. Short wavelengths below 500 nm are mostly attenuated in the front side of the cell device. Then, the disparity in terms of transmitted field intensities is more pronounced for light wavelengths longer than 600 nm.

It is clearly noticed that ultrathin SQW (2.5 nm) yields the highest propagating optical field across the back AZO to escape from the corresponding semi-transparent cell. However, ultrathin MQW (6 × 2.5 nm) configuration leads to higher transmitted optical field than the thin SQW (20 nm) with the same total absorber thickness. This can be attributed to both the reduction of a-Ge absorbing material amount at the expense of a-Si barrier layers and the increase of ultrathin QW bandgap relative to thin SQW. Consequently, the optical modelling results of the electric field estimate an intermediate transparency level of semi-transparent device with MQW (6 × 2.5 nm), considerably higher than thin SQW (20 nm) and closer to ultrathin SQW (2.5 nm).

Figure 4 presents the variations of local absorption as a function of wavelengths in semi-transparent solar cells with different QW nanoabsorber configurations. Considering the results presented in

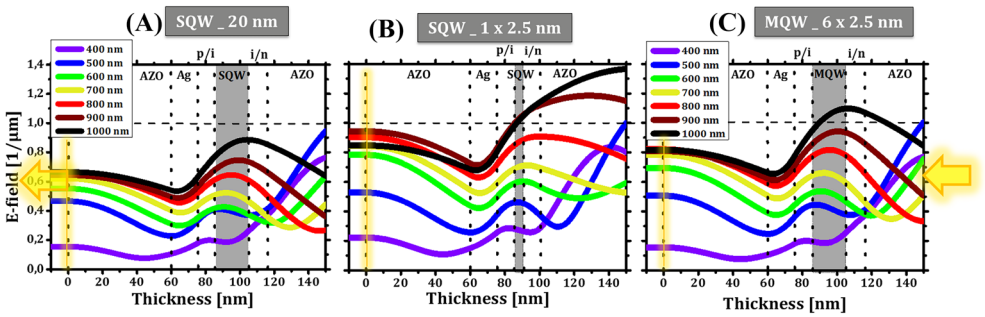


**FIGURE 3** Electric field intensities variation at selected wavelengths across the depth of semi-transparent solar cell devices for different nanoabsorber configurations: (A) thin SQW (20 nm), (B) ultrathin SQW (2.5 nm) and (C) ultrathin MQW of (6 × 2.5 nm). The highlighted dashed line in yellow points out the interface between the outermost back-electrode surfaces and the surrounding air. The yellow arrows on the right and the on the left sides of the graphs indicate the incident light and the transmitted light, respectively. [Colour figure can be viewed at wileyonlinelibrary.com]

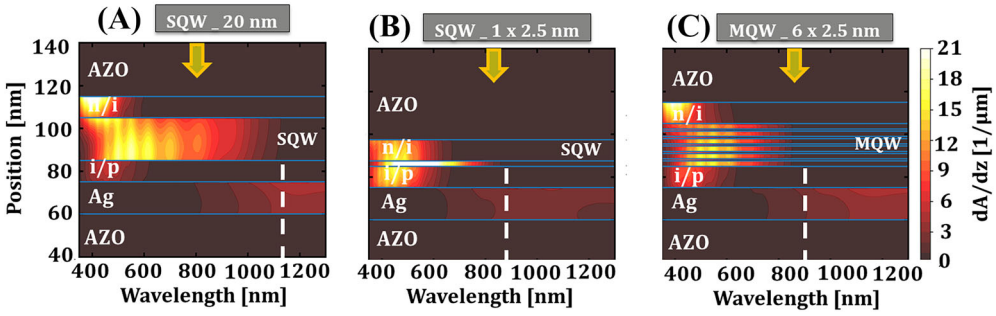


**FIGURE 4** Cross-sectional map of local absorption as a function of wavelengths in semi-transparent solar cells with different nanoabsorber configurations: (A) thin SQW (20 nm), (B) ultrathin SQW (2.5 nm) and (C) ultrathin MQW (6 × 2.5 nm). The dashed lines point out the absorption threshold wavelength for each nanoabsorber configuration. Yellow arrows point out the direction of the incident light. [Colour figure can be viewed at wileyonlinelibrary.com]

Figures 2 and S1, an overlapping of electric field maxima with the range of high refractive indices in the photoactive material is desired to promote and light absorption, according to Equation (1).[26]

Given the superior refractive indices of a-Ge QW compared with a-Si QB, higher local absorption is distinguished in all QW regions compared with the barrier zones. This points out the dominant contribution of the absorption in a-Ge QW in the photogeneration.[26]

Along the depth of solar cell devices, the regions of QW nanoabsorber in the vicinity of the Ag back electrodes are characterized by stronger local absorption in all the QW configuration. In particular, a gradual decrease in the absorption intensity is visualized over the stratified MQW structure, when QWs get away from the back contact.

One important note is that the absorption edge shifts towards shorter wavelength for both ultrathin SQW and MQW with reducing the corresponding QW thickness in contrast to thin SQW, as highlighted by the dashed white lines. This is expected to directly affect the profile of EQE spectra of the semi-transparent solar cells.

The resonance condition corresponding to the maximum absorption and minimum reflection is typically altered by the change of the optical nanocavity length and effective refractive index of the composing media. This is mainly due to change in the round-trip propagation phase shift.[26] Therefore, a red shift is expected when increasing the thickness of the optical nanocavity in the case of MQW (6 × 2.5 nm) and SQW (20 nm) compared with SQW (2.5 nm).

Experimentally, further enhancement of the optical absorption efficiency can be expected in ultrathin QW with smaller exciton Bohr radius due to larger binding energy and higher optical oscillator strength. These spatial confinement conditions promote the coupling between photons and confined charge carriers.[26]

High parasitic absorption can be noticed within the carrier-selective contact regions, in particular on the front side, which suggests a favourable replacement with wide-bandgap metal oxides to enhance both the photocurrent and the transparency of such QW-based ST-PV.[9,10] Another important specification of our semi-transparent QW PV technology is the angle insensitive behaviour of the absorbing resonance in the optical nanocavity. This is mainly due to the high absorption and subwavelength dimension of a-Si:H/a-Ge:H photonic resonator media, leading to a cancellation of the negligible round-trip propagation phase shift by reflection phase shifts.[40,41]

To this end, ultrathin MQW configuration provides effective optical absorption for photogeneration process and considerable visible transmission for lighting control. This allows to optically combine the benefits and alleviate the drawbacks of both thin and ultrathin SQW configurations.

### 3.3 | Electronic modelling of semi-transparent ultrathin Si/Ge MQW solar cell

Herein, using numerical simulation, we elucidate the impact of QC-tunable bandgap on the electronic characteristics of semi-transparent ultrathin Si/Ge QW solar cells. Figure 5 illustrate the energy band diagrams at open-circuit condition for different QW architectures.

A narrow bandgap (Eg ∼ 1 eV) is attributed to thin SQW (∼ 20 nm), whereas wider bandgap (Eg ∼ 1.35 eV) is assigned to both ultrathin SQW (2.5 nm) and MQW (6 × 2.5 nm) configurations.[24] Given the direct dependence of the supplied voltage by solar cell device on the nanoabsorber bandgap, a significant rise in photovoltage is estimated for both ultrathin SQW (2.5 nm) and MQW (6 × 2.5 nm) compared with thin SQW (∼ 20 nm). The increase of Voc for thinner QWs can be clearly seen in the large spatial splitting between the quasi-Fermi levels of electrons ($E_{F,n}$) and holes ($E_{F,p}$) due to the bandgap widening under QC effects.[42] In the simulation, a slightly lower Voc is determined for MQW (6 × 2.5 nm) with respect to SQW (2.5 nm). This is most likely caused by the multiplication of the recombination sites at each QW/barrier heterointerface.

Another important implication of quantum-size effects is the minimization of the conduction band discontinuity (ΔEc) at the QW/QB heterojunction when QW thickness is reduced. Therefore, large band offset (ΔEc ∼ 0.62 eV) is resulted from SQW (20 nm), whereas small band offsets (ΔEc ∼ 0.25 eV) are acquired in both ultrathin SQW (2.5 nm) and ultrathin MQW (6 × 2.5 nm).[25] This change in the potential barrier height at QW/QB heterointerface would affect the carrier collection through the escape transport by tunnelling and thermal emission mechanisms.[43] Hence, an enhancement in FF of the solar cell

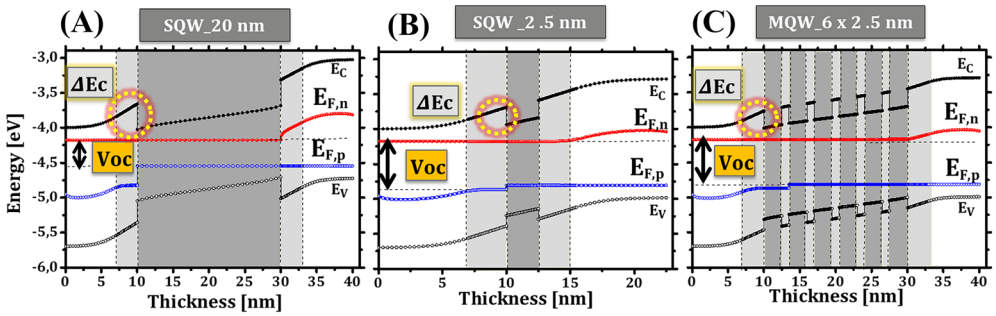


**FIGURE 5** Energy band diagrams at open-circuit condition for each semi-transparent n-i-p solar cell with different QW configurations: (A) SQW of 20 nm, (B) SQW of 2.5 nm and (C) MQW of 6 × 2.5 nm. The determined Voc parameters for different QW configurations are indicated by black arrows. The conduction band offsets ΔEc at QW/QB heterointerface are highlighted by dotted yellow circles. QW layers correspond to dark grey zones, while QB regions are filled with bright grey. [Colour figure can be viewed at wileyonlinelibrary.com]

devices with ultrathin SQW (2.5 nm) and MQW (6 × 2.5 nm) compared with thin SQW (20 nm) is expected.[44]

To gain further insights on MQW device operation via numerical modelling, a future analysis of the collective microscopic behaviour of charge carriers is considered as a prospective outlook. Therefore, the study of the spatial profiles for electron and hole densities in the intrinsic region as a depletion zone would allow the determination of all carrier dynamics in the MQW, including transport, generation and recombination.[45,46]

### 3.4 | Experimental characteristics of semi-transparent Si/Ge MQW solar cell

Considering the previously discussed outcomes of the optoelectronic modelling, we analyse the experimental performance outputs of the fabricated semi-transparent QW solar cell devices.

Figure 6A presents the EQE spectra of ultrathin MQW (6 × 2.5 nm) compared with ultrathin SQW (2.5 nm), thin SQW (∼ 20 nm) and full a-Si nanoabsorber (20 nm). On the one hand, it is clearly observed that MQW (6 × 2.5 nm) configuration enables a notable improvement in EQE compared with ultrathin SQW (2.5 nm) over the entire spectrum range (indicated by red arrows). Based on the aforementioned optical modelling results, this is attributed to the extension of the volume of photoactive medium and the increase of the absorbance by the multiplication of the QWs number. On the other hand, the EQE of MQW (6 × 2.5 nm) reaches similar level as thin SQW (20 nm) in the absorption range of short wavelengths below 600 nm, implying the add-up of photocurrent contributions from all the QWs. However, a deviation at long wavelength range is imposed by the absorption edge compared with thin SQW (20 nm) due to the bandgap widening under QC effects (indicated by blue arrows). This behaviour is in accordance with the outcomes of local absorption modelling in Figure 4.

The characteristic absorption resonance (maximum absorption) related to QW solar cells featuring subwavelength optical nanocavity is also shifted towards longer wavelength for MQW (6 × 2.5 nm) and SQW (20 nm) compared with SQW (2.5 nm). This is due to the change of the propagation phase shift controlled by the thickness and the effective refractive indices of the photonic resonator.[26] In the fabricated ultrathin MQW material system, it is assumed that the absorption efficiency is enhanced relative to thin SQW due to the increase of light interaction with confined carriers under quantum-size effects.[26] Conversely, the multiplication of QW/QB heterointerfaces inducing electronic states and strain can weaken the optical oscillator strength and, hence, the absorption efficiency.[28,47]

It is noteworthy that a slight deviation of the absorption threshold is noticed between ultrathin SQW (2.5 nm) and MQW (6 × 2.5 nm), which can be due to a relative bandgap difference. In real conditions, it is anticipated that the bandgap widening would be relatively less pronounced in MQW (6 × 2.5 nm) compared with SQW (2.5 nm), implying a slight shift in the absorption onset.[44,48] This can be due to the impact of heterointerface states on quantum confined system[28,47,49] and the change of the exciton effective mass under interface potentials.[49,50] Also, MQW configuration with ultrathin barrier tends to form superlattice-like band structure, where a tendency of wavefunction overlapping between adjacent a-Ge QWs can result in weaker QC and lower bandgap widening.[22] Furthermore, the thinnest SQW (2.5 nm) yields higher and broader EQE than a nanoabsorber composed of full a-Si (20 nm). This points out the superior absorption efficiency of a-Ge QW relative to even an order of magnitude-thicker a-Si layer.

Figure 6B shows the J-V curves under illumination for different semi-transparent QW solar cells. The corresponding cell performance characteristics are summarized in Table 1.

The short-circuit current values are in correlation with the EQE results, giving an intermediate photocurrent value for the MQW configuration (Jsc = 10.3 mA/cm$^2$) relative to ultrathin SQW-2.5 nm (Jsc = 4.7 mA/cm$^2$) and thin SQW-20 nm (Jsc = 15.5 mA/cm$^2$), whereas the device with a-Si nanoabsorber-20 nm delivers a low photocurrent current level, even below ultrathin SQW-2.5 nm. It is worthy to mention that the photocurrent delivered by semi-transparent solar cell with MQW nanoabsorber of about only 20 nm is within the range of photocurrent from ST-PV technology based on hundreds-of-nanometres-thick a-Si absorbers.[7,8] A dedicated study in future on the photocurrent evolution as a function of different QW numbers would be insightful to determine the generalized design rules. This would enable to correlate the change of nanocavity length to the optical field distribution and the local absorption in each individual QW.[26]

Regarding the other electronic characteristics, thin SQW (20 nm) device suffers from poor Voc and FF, due to low bandgap and transport obstruction by the large potential barriers. Also, the extension of

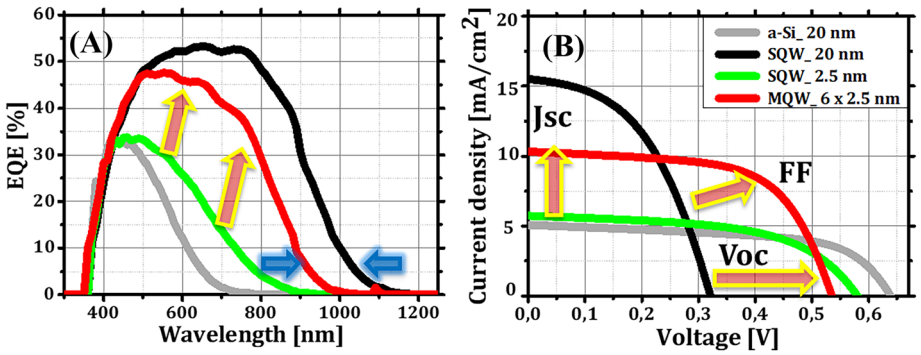


**FIGURE 6** Experimental outputs of semi-transparent devices with MQWs (6 × 2.5 nm) compared with ultrathin SQW (2.5 nm), thin SQW (20 nm) and full a-Si nanoabsorber (20 nm). (A) EQE and (B) illuminated J-V curves [Colour figure can be viewed at wileyonlinelibrary.com]

| Nanoabsorber | Jsc(mA/cm$^2$) | Voc (mV) | FF(%) | PCE(%) | AVT(%) | LUE(%) |
|---|---|---|---|---|---|---|
| a-Si (20 nm) | 4.9 | 645 | 60 | 1.97 | 30 | 0.6 |
| SQW (20 nm) | 15.5 | 320 | 47 | 2.33 | 25 | 0.58 |
| SQW (2.5 nm) | 5.4 | 580 | 59 | 1.89 | 39 | 0.73 |
| MQW (6 × 2.5 nm) | 10.3 | 535 | 61 | 3.41 | 33 | 1.12 |

**TABLE 1** Illuminated J-V outputs of semi-transparent solar cell devices with different nanoabsorbers

Abbreviations: FF, fill factor; Jsc, short-circuit current; LUE, light utilization efficiency; PCE, the photoconversion efficiency $PCE = \frac{Jsc \times Voc \times FF}{Pin}$ with pin: Input power; Voc, open-circuit voltage; VT, average visible transmission.

the recombination volume in thin QW can detrimentally affect the carrier travel, the scattering dynamics and the lifetime of the charge carriers, causing electronic deficiencies.[51] This can be alleviated by reducing the QW thickness in both ultrathin SQW (2.5 nm) and MQW (6 × 2.5 nm), owing to the bandgap widening and the minimization of the band offset at QW/barrier heterojunction.

First, the implementation of ultrathin MQW (6 × 2.5 nm) enables to overcome the Voc drawback related to thin SQW (20 nm), leading to an enhancement of Voc from 320 to 535 mV. This is in good agreement with the estimated simulation results, as shown in Figure 5, whereas the MQW (6 × 2.5 nm) preserves a comparable Voc level to ultrathin SQW (2.5 nm) because of quantum-size effect. The slight difference can be attributed to the multiplication of the recombination sites at the QW/barrier heterointerfaces in the case of MQW in contrast to the SQW.

Second, the bandgap engineering in the ultrathin MQW configuration facilitates the escape of the photogenerated carriers from the QWs to contribute in the photocurrent and mitigates the recombination processes. This promotes the collection efficiency of charge carriers flowing through the QW and reduces the transport hindering.[45,52,53] Therefore, a significant improvement in FF is achieved for MQW (6 × 2.5 nm) compared with thin SQW (20 nm) counterpart, from 47% up to 61%. This confirms the enhancement of the carrier transport and the lowering of resistive losses, due to the reduction of the conduction band discontinuity $\Delta$EC, as illustrated in Figure 5.

Overall, MQW configuration allows the combination of the benefits from both thin and ultrathin SQW counterparts. This is attributed to the rise of the photocurrent due to the extension of the volume of photoactive medium, as well as the enhancement of both Voc and FF thanks to the band gap engineering. Importantly, the semi-transparent MQW solar cell yields a PCE = 3.4%, which is largely superior to all other configurations. Relative improvements of about 73%, 41% and 67% are achieved relative to ultrathin SQW (2.5 nm), thin SQW (20 nm) and a-Si (20 nm), respectively.

It is important to mention that, according to detailed balance model, the optimum bandgap regime deviates to wider values as the visible transmission increases.[54] Therefore, the bandgap widening of a-Ge:H QW from ~1 to ~1.35 eV by thickness reduction due to QC effects agrees with this recommended trend.

Further optimization can be realized through the modulation of optical design and bandgap engineering, as well as by heterointerface post-treatments during the fabrication process. The back electrode is also an important component for the collection and transport mechanisms of charge carriers, which can potentially enhance FF. The change of Ag content or AZO surface termination and oxidation during the deposition processes lead to different work function and band alignment combinations.[55,56] This can reduce the recombination sites at semiconductor/Ag interface under sputtering damage and can also minimize the potential barrier at Ag/ZnO interface, controlling charge transfer and electrical conductivity. Thus, we estimate that a realistic practical efficiency above 4% can be potentially achieved for such semi-transparent MQW PV.

Figure 7 presents the transmission and reflection spectra for different semi-transparent devices with and without metal/oxide (MO) transparent electrodes. The semi-transparent device with MQW (6 × 2.5 nm) presents higher transmission and lower reflection levels than both thin SQW (20 nm) and a-Si (20 nm), while it still reaches comparable optical performance to ultrathin SQW (2.5 nm). Counterintuitively, higher transmission and lower reflection are obtained for all semi-transparent cells with adding back electrode compared with bare back side. The main reason for the alteration in the optical transmission and reflection by introducing MO electrode is the difference in refractive indices between ($n_{Ag} \sim 0$) and ($n_{air} \sim 1$). As discussed in Section S3, higher difference between the refractive index of the front and the back electrodes ($n_{front} - n_{back}$) is beneficial to maximize the optical absorption at the expense of reflection lowering.[13,35] In this regard, ($n_{AZO,front} - n_{Ag,\ back}$) is higher than ($n_{AZO,front} - n_{Air,\ back}$), leading to reduced reflection of the full semi-transparent cells (front AZO/n-i-p/Ag/back AZO) with MO back contact compared with (front AZO/n-i-p/air) with bare back side. It is well known that at normal incidence, a maximum absorption can be linked to ($n_{front}$ / $n_{front} + n_{back}$), which gets lower in the case of air compared with MO back electrode for ST-PV with different nanoabsorber configurations.

However, a clear disparity is noticed in the optical gain provided by the implementation of transparent Ag/AZO back electrodes in different semi-transparent solar cell devices. In this context, the largest improvement is obtained for MQW (6 × 2.5 nm) and then for SQW (20 nm), but a slight change is observed in a-Si (20 nm) and SQW (2.5 nm) structures. It can be directly noticed that that the enhancement of transmission is directly related to a decrease in reflection. The minimum reflection corresponds to the absorption resonance condition owing to the recurrence of optical interferences between incident and reflected light. Since the reflection phase shift at the front remains similar for all semi-transparent device configurations,

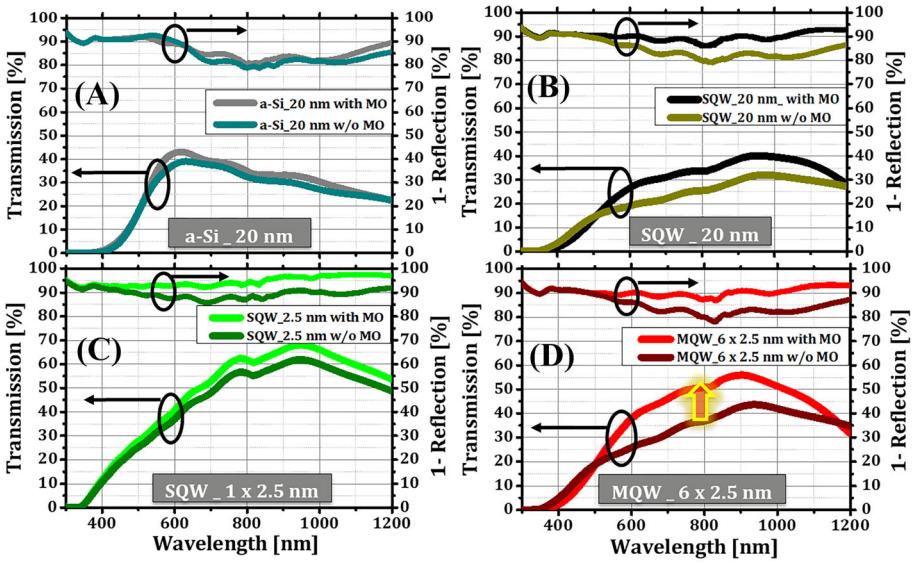


**FIGURE 7** Experimental transmission and (1-reflection) spectra for different semi-transparent QW solar cells with and without metal/oxide (MO) back electrode. (A) a-Si nanoabsorber (20 nm). (B) Thin SQW (20 nm), (C) ultrathin SQW (2.5 nm) and (D) MQW (6 × 2.5 nm). The largest gain in transmission spectra with the introduction of MO electrode in MQW (6 × 2.5 nm) is indicated by red arrow. [Colour figure can be viewed at wileyonlinelibrary.com]

such resonance condition is rather controlled by the reflection phase shift at the back side and the round-trip propagation phase shift within the photonic resonator, as explained in Section S3. Therefore, for each semi-transparent solar cell device, the change of the thickness and refractive index of the absorbing n-i-p region alters the transmission and reflection behaviour, when changing the refractive index of the back electrode from $n_{air}$ to $n_{Ag}$.

As an experimental indication of the relationship between the transmission enhancement and the reflection change in the case of MQW (6 × 2.5 nm), a clear shift of transmission maxima and similarly (1-reflection) minima towards shorter wavelength is noticed using metal/oxide transparent back electrode compared with bare back side. This shifting effect is more pronounced in the case of MQW (6 × 2.5 nm) and then for SQW (20 nm) but insignificant in a-Si (20 nm) and SQW (2.5 nm) structures. Therefore, the substantial reduction of reflection in MQW (6 × 2.5 nm) with metal/oxide transparent back electrode compared with bare back side due to the modulation of the optical interference and the nanocavity resonance mode is the main reason of the large enhancement of transmission in contrast to other semi-transparent device counterparts.

Among physical parameters, temperature is an important factor determining the structural and optoelectronic properties of functional semiconductor layers, considering possible hydrogen dynamics within hydrogenated amorphous materials.[57,58] For our ultrathin QW solar cell technology, temperature effect can be manifested on three different levels: temperatures of PECVD deposition processes, temperature of post-deposition annealing and temperature variation during solar cell device operation. A discussion about the temperature effect on transmission and power conversion efficiency at different technological stages of semi-transparent MQW solar cell considering possible hydrogen dynamics within hydrogenated amorphous materials is addressed in Section S5.

Also, it is important to consider that surface hydrogenation could induce metallization in different semiconductors leading to spatially confined electrical conduction at the semiconductor nanoscale.[59–63] This could potentially influence the electronic transport of charge carriers and the optical reflection. Specific mechanisms are required hydrogen-induced metallization which are altered according to the particularity of semiconductor surfaces in terms of physical and electronic structure as well as hydrogen adsorption.[59,64–66] However, the role of hydrogen during hydrogenated amorphous a-Si:H and a-Ge:H growth processes and upon post-deposition thermal treatment consists mainly in passivation of dangling bonds[67,68] and in the disorder-to-order transitions inducing crystallization.[57,69,70] These mechanisms provide better optoelectronic properties and film quality just below the onset of amorphous-to-nanocrystalline transition regime.[57,67] Hence, there is no clear evidence of hydrogen-induced metallization neither in our a-Si:H/a-Ge:H multilayer system nor from literature.[5,7,9,10,41,57]

Figure 8A displays a visual image of the contrast between full semi-transparent cells (front AZO/n-i-p/Ag/back AZO) with MO back electrode compared with (front AZO/n-i-p/air) with bare back side. The areas with MO contact defined by square look more transparent and the underlying logos appear visibly clearer and bolder, compared with the remaining surface area.

Based on the transmission spectra of semi-transparent cell shown in Figure 7, we determine the average visible transmission as a conventional figure-of-merit for the assessment of ST-PV. This parameter is defined as the integration of the transmission spectrum and AM 1.5G photon flux weighted with the photopic response of the human eye, as follows[30]:

$$AVT = \frac{\int T(\lambda)P(\lambda)AM1.5G(\lambda)d\lambda}{\int P(\lambda)\,AM1.5G(\lambda)d\lambda}, \quad (2)$$

where λ is the wavelength, $T$ is the transmittance through PV device, $P$ is the photopic luminosity function for the response of the human eye and $AM1.5G$ (λ) is photon flux under AM 1.5G light illumination

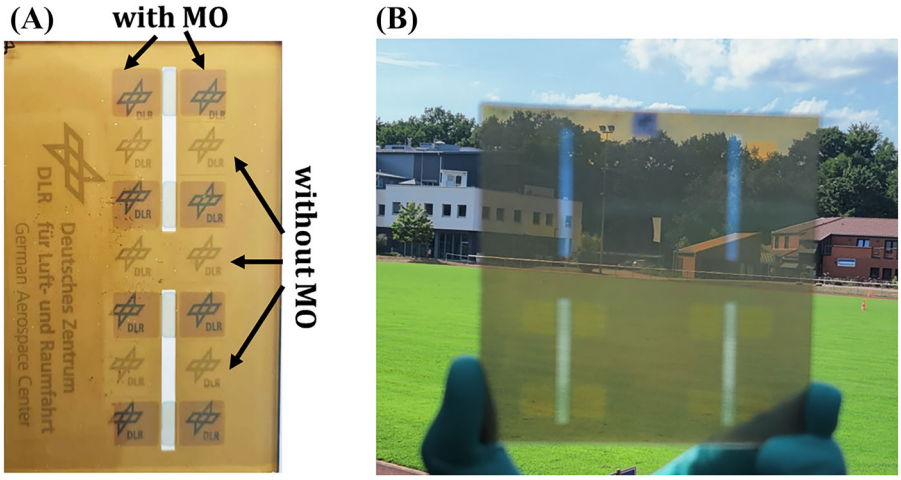


**FIGURE 8** (A) Photograph of semi-transparent structure featuring MQW (6 × 2.5 nm) nanoabsorber. The square shapes are the cores of full semi-transparent cells (front AZO/n-i-p/Ag/back AZO) with metal/oxide MO back electrode. The remaining area is composed of (front AZO/n-i-p/air) with bare back side. The white paper in the background can induce double pass of light, which is assumed to intensify the tint appearance and the contrast between different regions. (B) Visual appearance of semi-transparent MQW (6 × 2.5 nm) structure with outdoor background. The open rectangles are laser scribing for front contact opening. [Colour figure can be viewed at wileyonlinelibrary.com]

conditions. Subsequently, the interplay between efficiency and visible transparency gives rise to an additional evaluation parameter, namely, light utilization efficiency (LUE), given by the product:

$$LUE = PCE \times AVT. \quad (3)$$

The AVT and LUE values for each semi-transparent QW device are reported in Table 1.On the optical visibility aspect, ultrathin MQW (6 × 2.5 nm) leads to higher AVT of about 33% than AVT around 25% for thin SQW (20 nm) with similar photoactive material thickness. This is consistent with the optical modelling of the transmitted optical field, shown in Figures 2 and 3.

A photograph of semi-transparent device structure with ultrathin MQW (6 × 2.5 nm) is shown in Figure 8B. Based on the corresponding transmission and reflection spectra, colour rendering index (CRI) as an aesthetic evaluation parameter can be determined.[30] The corresponding CRI of semi-transparent device with ultrathin MQW device is closer to 70%. The cell appears with a pale yellowish tint corresponding to coordinates $(x, y) = (0.43,42)$ in the CIE chromaticity diagram. This is in accordance with the aesthetic characteristics of non-wavelength-selective thinned absorbers, based on related detailed balance model.[54]

Surprisingly, in spite of the multiplication of QWs, a remarkable AVT level is ensured in the case of MQW closer to ultrathin SQW (2.5 nm) counterpart with AVT up to 39%. To the best of our knowledge, the device with ultrathin SQW (2.5 nm) is the thinnest semi-transparent QW solar cell reported in literature so far. Moreover, both ultrathin SQW (2.5 nm) and MQW (6 × 2.5 nm) are more advantageous in terms of achieving high visible transmission than full a-Si nanoabsorber (20 nm).

It is worthy to mention that MQW concept provides an extra degree of freedom in the optical management that could allow to tune the transparency and to improve the photocurrent of semi-transparent solar cell. This could be achieved via the adjustment of design of MQW configurations with different positions, numbers and thicknesses. In addition, the thickness adjustment of Ag/AZO bilayer allows a considerable tuning of the AVT and CRI attributes. This can enable a good control of the aesthetic and the lightning of semi-transparent QW PV technology.

Interestingly, MQW (6 × 2.5 nm) yields a striking boost in LUE exceeding 1.1%, compared with thin (LUE = 0.58%) and ultrathin (LUE = 0.73%) SQW counterparts. This LUE level can be considered as higher than most of other semi-transparent inorganic technologies in the state of the art and close the record among inorganic counterparts (~1.3%).[7]

To this end, the integration of MQW as nanoabsorber in novel semi-transparent ultrathin Si/Ge solar cell allows to overcome the physical limitations of SQW counterparts, that is, low absorbance for ultrathin SQW and inappropriate electronic structure for the thin SQW. The bandgap engineering and optical design features enable an optimum trade-off between efficiency and transparency, by enhancing the power generation performance while preserving a considerably high visible transmission level.

## 4 | CONCLUSIONS

In this work, we report the prime proof of concept for a novel semi-transparent solar cell based on multiple QWs as ultrathin nanoabsorber. The here presented semi-transparent device concept employing amorphous Si/Ge quantum confined nanostructures integrated in a subwavelength nanophotonic resonator is unique of its kind. This MQW architecture enables the improvement of PV performance owing to extra degree of freedom in both photonic management and bandgap engineering, rather than just thinning approach.

The aim of the multiplication of QWs in a configuration of 6 × 2.5 nm is to overcome the intrinsic limitations imposed by single QW configurations, mainly the low absorbance for ultrathin SQW (2.5 nm) and the inappropriate electronic structure for thin SQW (20 nm).

Based on optical modelling of the electric field and the local absorption distributions, the improvement of photocurrent and the maintaining of high transmission in MQW (6 × 2.5 nm) with respect to ultrathin SQW (2.5 nm) are explained. The impact of the threshold absorption difference between MQW (6 × 2.5 nm) and thin SQW (20 nm) on the EQE deviation and the photocurrent level is analysed.

According to electrical simulation, the bandgap widening and the minimization of QW/QB conduction band offset under QC effects are determined as the main reasons for higher Voc and FF in ultrathin SQW (2.5 nm) and MQW (6 × 2.5 nm) compared with thin SQW (20 nm). Therefore, such emerging semi-transparent MQW PV technology takes advantage of an effective synergy between quantum and photonic confinements to boost both the power generation and visible transmission levels, achieving an optimum trade-off between efficiency and transparency. In addition, the design rules for further improvement through spectral and bandgap engineering are indicated.

Overall, the main output of this work is the experimental demonstration of the effectiveness of amorphous Si/Ge MQW concept in boosting the power conversion efficiency of about 3.4%, while preserving a considerable average visible transmission level around 33%. A corresponding light utilization efficiency above 1.1% is achieved, which can be considered as one of the highest among inorganic semi-transparent solar cell technologies. The current demonstration of ultrathin semi-transparent MQW PV technology points out the promising potential for integration in relevant applications such as in buildings, vehicles and greenhouses.

## ACKNOWLEDGEMENTS

H.M., M.G.-K., K.G. and M.V. acknowledge funding from the Energy branch of the German Aerospace Center (DLR). They would also like to thank N. Osterthun, U. Banik, L. Busch, N. Neugebohrn, O. Sergeev and all the group colleagues at DLR-VE Institute of Networked Energy Systems for the insightful scientific inputs. C.F. and M.S. are funded by the Deutsche Forschungsgemeinschaft (DFG, German Research Foundation) – 217133147/SFB 1073, project B02. The use of equipment of the "Collaborative Laboratory and User Facility for Electron Microscopy" (CLUE, Göttingen) is gratefully acknowledged.

## DATA AVAILABILITY STATEMENT

The data that support the findings of this study are available on request from the corresponding author. The data are not publicly available due to privacy or ethical restrictions.

## REFERENCES

1. Meddeb H, Götz-Köhler M, Neugebohrn N, et al. Tunable photovoltaics: adapting solar cell technologies to versatile applications. *Adv Energy Mater*. 2022;12(28):2200713. doi:10.1002/aenm.202200713
2. Li Z, Ma T, Yang H, Lu L, Wang R. Transparent and colored solar photovoltaics for building integration. *Sol RRL*. 2021;5(3):2000614. doi:10.1002/solr.202000614
3. Traverse CJ, Pandey R, Barr MC, Lunt RR. Emergence of highly transparent photovoltaics for distributed applications. *Nat Energy*. 2017;2(11):849-860. doi:10.1038/s41560-017-0016-9
4. Zhao Y, Zhu Y, Cheng H-W, Zheng R, Meng D, Yang Y. A review on semitransparent solar cells for agricultural application. *Materials Today Energy*. 2021;22:100852. doi:10.1016/j.mtener.2021.100852
5. Lee K, Um H-D, Choi D, et al. The development of transparent photovoltaics. *Cell Rep Phys Sci*. 2020;1(8):100143. doi:10.1016/j.xcrp.2020.100143
6. Massiot I, Cattoni A, Collin S. Progress and prospects for ultrathin solar cells. *Nat Energy*. 2020;5(12):959-972. doi:10.1038/s41560-020-00714-4
7. Almora O, Baran D, Bazan GC, et al. Device performance of emerging photovoltaic materials (version 2). *Adv Energy Mater*. 2021;11(11):2102526. doi:10.1002/aenm.202102526
8. Cho J-S, Seo YH, Lee A, et al. Energy-harvesting photovoltaic transparent tandem devices using hydrogenated amorphous and microcrystalline silicon absorber layers for window applications. *Appl Surf Sci*. 2022;589:152936. doi:10.1016/j.apsusc.2022.152936
9. Kim S, Patel M, Nguyen TT, Yi J, Wong C-P, Kim J. Si-embedded metal oxide transparent solar cells. *Nano Energy*. 2020;77:105090. doi:10.1016/j.nanoen.2020.105090
10. Kim S, Patel M, Nguyen TT, Kumar N, Bhatnagar P, Kim J. Highly transparent bidirectional transparent photovoltaics for on-site power generators. *ACS Appl Mater Interfaces*. 2022;14(1):706-716. doi:10.1021/acsami.1c18473
11. Lopez-Garcia AJ, Blazquez O, Voz C, Puigdollers J, Izquierdo-Roca V, Pérez-Rodríguez A. Ultrathin wide-bandgap a-Si:H-based solar cells for transparent photovoltaic applications. *Sol RRL*. 2022;6(1):2100909. doi:10.1002/solr.202100909
12. Kats MA, Blanchard R, Genevet P, Capasso F. Nanometre optical coatings based on strong interference effects in highly absorbing media. *Nat Mater*. 2013;12(1):20-24. doi:10.1038/nmat3443
13. Kats MA, Capasso F. Optical absorbers based on strong interference in ultra-thin films. *Laser Photonic Rev*. 2016;10(5):735-749. doi:10.1002/lpor.201600098
14. Steenhoff V, Theuring M, Vehse M, von Maydell K, Agert C. Ultrathin resonant-cavity-enhanced solar cells with amorphous germanium absorbers. *Adv Opt Mater*. 2015;3(2):182-186. doi:10.1002/adom.201400386
15. Götz M, Osterthun N, Gehrke K, Vehse M, Agert C. Ultrathin nano-absorbers in photovoltaics: prospects and innovative applications. *Coatings*. 2020;10(3):218. doi:10.3390/coatings10030218
16. Götz M, Lengert M, Osterthun N, Gehrke K, Vehse M, Agert C. Switchable photocurrent generation in an ultrathin resonant cavity solar cell. *ACS Photonic*. 2020;7(4):1022-1029. doi:10.1021/acsphotonics.9b01734
17. Gotz-Kohler M, Meddeb H, Gehrke K, Vehse M, Agert C. Ultrathin solar cell with magnesium-based optical switching for window applications. *IEEE J Photovolt*. 2021;11(6):1388-1394. doi:10.1109/JPHOTOV.2021.3110311
18. Götz-Köhler M, Banik U, Meddeb H, et al. Switchable photovoltaic window for on-demand shading and electricity generation. *Sol Energy*. 2022;232:433-443. doi:10.1016/j.solener.2021.12.071
19. Osterthun N, Neugebohrn N, Gehrke K, Vehse M, Agert C. Spectral engineering of ultrathin germanium solar cells for combined photovoltaic and photosynthesis. *Opt Express*. 2021;29(2):938-950. doi:10.1364/OE.412101
20. Barbagiovanni EG, Lockwood DJ, Simpson PJ, Goncharova LV. Quantum confinement in Si and Ge nanostructures: theory and experiment. *Appl Phys Rev*. 2014;1(1):11302. doi:10.1063/1.4835095

21. Wang X-D, Wang H-F, Chen B, Li Y-P, Ma Y-Y. A model for thickness effect on the band gap of amorphous germanium film. *Appl Phys Lett*. 2013;102(20):202102. doi:10.1063/1.4805056
22. Liu P, Longo P, Zaslavsky A, Pacifici D. Optical bandgap of single- and multi-layered amorphous germanium ultra-thin films. *J Appl Phys*. 2016;119(1):14304. doi:10.1063/1.4939296
23. Cosentino S, Miritello M, Crupi I, et al. Room-temperature efficient light detection by amorphous Ge quantum wells. *Nanoscale Res Lett*. 2013;8(1):128. doi:10.1186/1556-276X-8-128
24. Meddeb H, Osterthun N, Götz M, et al. Quantum confinement-tunable solar cell based on ultrathin amorphous germanium. *Nano Energy*. 2020;76:105048. doi:10.1016/j.nanoen.2020.105048
25. Meddeb H, Osterthun N, Gotz M, Sergeev O, Gehrke K, Vehse M, Agert C. Quantum well solar cell using ultrathin germanium nanoabsorber. In: *2020 47th IEEE Photovoltaic Specialists*, pp. 1149–1152.
26. Meddeb H, Gotz-Kohler M, Osterthun N, et al. Investigation of quantum size effects on the optical absorption in ultrathin single quantum well solar cell embedded as a nanophotonic resonator. *IEEE J Photovolt*. 2022;12(3):1-11. doi:10.1109/JPHOTOV.2022.3150726
27. Cosentino S, Barbagiovanni EG, Crupi I, et al. Size dependent light absorption modulation and enhanced carrier transport in germanium quantum dots devices. *Solar Energy Mater sol Cell*. 2015;135:22-28. doi:10.1016/j.solmat.2014.09.012
28. Cosentino S, Sungur Ozen E, Raciti R, et al. Light harvesting with Ge quantum dots embedded in $SiO_2$ or $Si_3N_4$. *J Appl Phys*. 2014;115(4):43103. doi:10.1063/1.4863124
29. Mirabella S, Cosentino S, Failla M, et al. Light absorption enhancement in closely packed Ge quantum dots. *Appl Phys Lett*. 2013;102(19):193105. doi:10.1063/1.4805356
30. Yang C, Liu D, Bates M, Barr MC, Lunt RR. How to accurately report transparent solar cells. *Joule*. 2019;3(8):1803-1809. doi:10.1016/j.joule.2019.06.005
31. WTheiss Hardware and software- CODE/Scout https://www.wtheiss.com/ (Accessed June 2022).
32. Varache R, Leendertz C, Gueunier-Farret ME, Haschke J, Muñoz D, Korte L. Investigation of selective junctions using a newly developed tunnel current model for solar cell applications. *Solar Energy Mater sol Cell*. 2015;141:14-23. doi:10.1016/j.solmat.2015.05.014
33. Raciti R, Bahariqushchi R, Summonte C, Aydinli A, Terrasi A, Mirabella S. Optical bandgap of semiconductor nanostructures: methods for experimental data analysis. *J Appl Phys*. 2017;121(23):234304. doi:10.1063/1.4986436
34. Lee K-T, Seo S, Lee JY, Guo LJ. Strong resonance effect in a lossy medium-based optical cavity for angle robust spectrum filters. *Adv Mater*. 2014;26(36):6324-6328. doi:10.1002/adma.201402117
35. Hägglund C, Apell SP, Kasemo B. Maximized optical absorption in ultrathin films and its application to plasmon-based two-dimensional photovoltaics. *Nano Lett*. 2010;10(8):3135-3141. doi:10.1021/nl101929j
36. Lee K-T, Seo S, Guo LJ. High-color-purity subtractive color filters with a wide viewing angle based on plasmonic perfect absorbers. *Adv Opt Mater*. 2015;3(3):347-352. doi:10.1002/adom.201400533
37. Behaghel B, Tamaki R, Vandamme N, et al. Absorption enhancement through Fabry-Pérot resonant modes in a 430 nm thick InGaAs/GaAsP multiple quantum wells solar cell. *Appl Phys Lett*. 2015;106(8):81107. doi:10.1063/1.4913469
38. Chen C-Y, Tan G-H, Hsu H-L, Chen C-P, Lin H-W. Recent progress on advanced optical structures for emerging photovoltaics and photodetectors. *Adv Energy Sustain Res*. 2020;1(1):2000035. doi:10.1002/aesr.202000035
39. Steenhoff V, Juilfs M, Ravekes R-E, et al. Optimized optical field profile in resonant-cavity-enhanced a-Ge:H nanoabsorber solar cells for tandem cell application. *IEEE J Photovolt*. 2017;7(1):3-10. doi:10.1109/JPHOTOV.2016.2617039
40. Lee K-T, Lee JY, Seo S, Guo LJ. Colored ultrathin hybrid photovoltaics with high quantum efficiency. *Light Sci Appl*. 2014;3(10):e215. doi:10.1038/lsa.2014.96
41. Lee JY, Lee K-T, Seo S, Guo LJ. Decorative power generating panels creating angle insensitive transmissive colors. *Sci Rep*. 2014;4(1):4192. doi:10.1038/srep04192
42. Wurfel U, Cuevas A, Wurfel P. Charge carrier separation in solar cells. *IEEE J Photovolt*. 2015;5(1):461-469. doi:10.1109/JPHOTOV.2014.2363550
43. Toprasertpong K, Goodnick SM, Nakano Y, Sugiyama M. Effective mobility for sequential carrier transport in multiple quantum well structures. *Phys Rev B*. 2017;96(7):075441. doi:10.1103/PhysRevB.96.075441
44. Meddeb H, Gotz-Kohler M, Osterthun N, Sergeev O, Gehrke K, Vehse M, Agert C. Ultrathin multiple quantum wells solar cell based on silicon/germanium nanostructures. In: *2021 IEEE 48th Photovoltaic Specialists*, pp. 975–978.
45. Toprasertpong K, Inoue T, Nakano Y, Sugiyama M. Investigation and modeling of photocurrent collection process in multiple quantum well solar cells. *Sol Energy Mater sol Cells*. 2018;174:146-156. doi:10.1016/j.solmat.2017.08.036
46. Toprasertpong K, Delamarre A, Nakano Y, Guillemoles J-F, Sugiyama M. Generalized reciprocity relations in solar cells with voltage-dependent carrier collection: application to p-i-n junction devices. *Phys Rev Applied*. 2019;11(2):024029. doi:10.1103/PhysRevApplied.11.024029
47. Mirabella S, Cosentino S, Gentile A, et al. Matrix role in Ge nanoclusters embedded in $Si_3N_4$ or $SiO_2$. *Appl Phys Lett*. 2012;101(1):11911. doi:10.1063/1.4734395
48. Almora O, Cabrera CI, Garcia-Cerrillo J, Kirchartz T, Rau U, Brabec CJ. Quantifying the absorption onset in the quantum efficiency of emerging photovoltaic devices. *Adv Energy Mater*. 2021;11(16):2100022. doi:10.1002/aenm.202100022
49. Cosentino S, Mio AM, Barbagiovanni EG, et al. The role of the interface in germanium quantum dots: when not only size matters for quantum confinement effects. *Nanoscale*. 2015;7(26):11401-11408. doi:10.1039/c5nr01480h
50. Barbagiovanni EG, Cosentino S, Lockwood DJ, Costa Filho RN, Terrasi A, Mirabella S. Influence of interface potential on the effective mass in Ge nanostructures. *J Appl Phys*. 2015;117(15):154304. doi:10.1063/1.4918549
51. Sandberg OJ, Sundqvist A, Nyman M, Österbacka R. Relating charge transport, contact properties, and recombination to open-circuit voltage in sandwich-type thin-film solar cells. *Phys Rev Applied*. 2016;5(4):044005. doi:10.1103/PhysRevApplied.5.044005
52. Nelson J, Paxman M, Barnham K, Roberts JS, Button C. Steady-state carrier escape from single quantum wells. *IEEE J Quantum Electron*. 1993;29(6):1460-1468. doi:10.1109/3.234396
53. Ramey SM, Khoie R. Modeling of multiple-quantum-well solar cells including capture, escape, and recombination of photoexcited carriers in quantum wells. *IEEE Trans Electron Dev*. 2003;50(5):1179-1188. doi:10.1109/TED.2003.813475
54. Wheeler LM, Wheeler VM. Detailed balance analysis of photovoltaic windows. *ACS Energy Lett*. 2019;4(9):2130-2136. doi:10.1021/acsenergylett.9b01316
55. Huang P-S, Qin F, Lee J-K. Role of the interface between Ag and ZnO in the electric conductivity of Ag nanoparticle-embedded ZnO. *ACS Appl Mater Interfaces*. 2020;12(4):4715-4721. doi:10.1021/acsami.9b17922
56. Chernysheva E, Srour W, Philippe B, et al. Band alignment at Ag/ZnO (0001) interfaces: a combined soft and hard X-ray photoemission study. *Phys Rev B*. 2018;97(23):235430. doi:10.1103/PhysRevB.97.235430
57. de Vrijer T, Ravichandran A, Bouazzata B, Smets AH. The impact of processing conditions and post-deposition oxidation on the opto-

electrical properties of hydrogenated amorphous and nano-crystalline germanium films. *J Non Cryst Solids*. 2021;553:120507. doi:10.1016/j.jnoncrysol.2020.120507

58. Yang Y, Yoon G, Park S, et al. Revealing structural disorder in hydrogenated amorphous silicon for a low-loss photonic platform at visible frequencies. *Adv Mater (Deerfield Beach, Fla)*. 2021;33(9):e2005893. doi:10.1002/adma.202005893
59. Derycke V, Soukiassian PG, Amy F, et al. Nanochemistry at the atomic scale revealed in hydrogen-induced semiconductor surface metallization. *Nat Mater*. 2003;2(4):253-258. doi:10.1038/nmat835
60. Cai Y, Bai Z, Pan H, Feng YP, Yakobson BI, Zhang Y-W. Constructing metallic nanoroads on a $MoS_2$ monolayer via hydrogenation. *Nanoscale*. 2014;6(3):1691-1697. doi:10.1039/c3nr05218d
61. Wang Y, Meyer B, Yin X, et al. Hydrogen induced metallicity on the ZnO(1010) surface. *Phys Rev Lett*. 2005;95(26):266104. doi:10.1103/PhysRevLett.95.266104
62. Kepenekian M, Robles R, Joachim C, Lorente N. Surface-state engineering for interconnects on H-passivated Si(100). *Nano Lett*. 2013;13(3):1192-1195. doi:10.1021/nl304611m
63. Bianco F, Bowler DR, Owen JHG, Köster SA, Longobardi M, Renner C. Scalable patterning of one-dimensional dangling bond rows on hydrogenated Si(001). *ACS Nano*. 2013;7(5):4422-4428. doi:10.1021/nn4010236
64. Trabada DG, Flores F, Ortega J. Hydrogenation of semiconductor surfaces: Si-terminated cubic SiC(100) surfaces. *Phys Rev B*. 2009;80(7):075307. doi:10.1103/PhysRevB.80.075307
65. Peng X, Krüger P, Pollmann J. Hydrogenated SiC(001)−(3×2) surface: semiconducting and metallic structures. *Phys Rev B*. 2007;76(12):125303. doi:10.1103/PhysRevB.76.125303
66. Mayne AJ, Riedel D, Comtet G, Dujardin G. Atomic-scale studies of hydrogenated semiconductor surfaces. *Progress Surf Sci*. 2006;81(1):1-51. doi:10.1016/j.progsurf.2006.01.001
67. Meddeb H, Bearda T, Abdelraheem Y, et al. Structural, hydrogen bonding and in situ studies of the effect of hydrogen dilution on the passivation by amorphous silicon of n-type crystalline (1 0 0) silicon surfaces. *J Phys D Appl Phys*. 2015;48(41):415301. doi:10.1088/0022-3727/48/41/415301
68. Meddeb H, Bearda T, Dimassi W, et al. Ultra high amorphous silicon passivation quality of crystalline silicon surface using in-situ post-deposition treatments. *Phys Status Solidi RRL*. 2015;9(1):53-56. doi:10.1002/pssr.201409494
69. Sriraman S, Agarwal S, Aydil ES, Maroudas D. Mechanism of hydrogen-induced crystallization of amorphous silicon. *Nature*. 2002;418(6893):62-65. doi:10.1038/nature00866
70. Roca i Cabarrocas P, Fontcuberta i Morral A, Kalache B, Kasouit S. Microcrystalline silicon thin-films grown by plasma enhanced chemical vapour deposition—growth mechanisms and grain size control. *SSP*. 2003;93:257-268. doi:10.4028/www.scientific.net/SSP.93.257

## SUPPORTING INFORMATION

Additional supporting information can be found online in the Supporting Information section at the end of this article.

**How to cite this article:** Meddeb H, Götz-Köhler M, Flathmann C, Seibt M, Gehrke K, Vehse M. Novel semi-transparent solar cell based on ultrathin multiple Si/Ge quantum wells. *Prog Photovolt Res Appl*. 2022;1-13. doi:10.1002/pip.3665